UNIVERSITY OF CALIFORNIA

Los Angeles

Exploring HOMER1 as a Postsynaptic Marker for Ribbon Synapses in the Peripheral Vestibular Epithelia

A thesis submitted in partial satisfaction

of the requirements for the degree Master of Science

in Physiological Science

by

Tyler Joseph Kramer

2024

ABSTRACT OF THE THESIS

Exploring HOMER1 as a Postsynaptic Marker for Ribbon Synapses in the Peripheral Vestibular Epithelia

by

Tyler Joseph Kramer

Master of Science in Physiological Science

University of California, Los Angeles, 2024

Professor Stephanie White, Chair

Ribbon synapses are one of the primary means of synaptic transmission within mammalian sensory systems. Loss of these synapses results in potential sensory dysfunction, as a result, their quantification is of critical importance to understanding the effects synaptic pathology may have on symptomatic sensory deficits. Immunohistochemistry is considered a reliable method to label these synapses, yet challenges arise when quantifying their distributions. In the vestibular periphery, low associations with standard postsynaptic markers and manual segmentation of these synapses have created significant barriers to our understanding of the relationship between changes in synapse density and its potential implications in pathology. The purpose of this study is to provide a novel method emphasizing rigorous analyses of immunolabeled ribbon synapses in the vestibular periphery, advancing our understanding of synapse distributions, and potential impacts various pathologies may have on these specialized structures.

The thesis of Tyler Joseph Kramer is approved.

Duncan Leitch

Felix Schweizer

Larry F. Hoffman

Stephanie White, Chair

University of California, Los Angeles

2024

INTRODUCTION

Sensory coding and transmission within the vertebrate inner ear are initiated by specialized hair cells, which upon mechanical displacement, convert audiovestibular stimuli into neural impulses with remarkable precision. Through a highly specialized synaptic architecture, these cells relay critical information to afferent neurons at rapid speeds, forming the essential neural pathways for hearing and balance. Two mechanisms of synaptic transmission exist within the neuroepithelia of the inner ear: nonquantal and quantal transmission. Nonquantal transmission (NQT) results from direct coupling of the hair cell and afferent within the vestibular epithelia, different than the direct coupling associated with gap junctions (Contini et al., 2016, 2022; Govindaraju et al., 2023; Holt et al., 2007; Songer and Eatock, 2013). Quantal transmission exists within both the cochlea and vestibular periphery utilizing specialized glutamatergic synapses referred to as ribbon synapses. These synapses, composed of a presynaptic "ribbon" within the hair cell and a glutamatergic postsynaptic density on afferent terminals, facilitate rapid transmission of sensory stimuli related to hearing, head rotation, or linear movement (Khan and Chang, 2013; Khimich et al., 2005; Voorns & Vogl, 2020; Zanazzi & Matthews, 2009). While the precise function of these ribbons is not fully understood, evidence suggests they are involved in directing, docking, and releasing of synaptic vesicles into the cleft (Voorns & Vogl, 2020; Zanazzi & Matthews, 2009).

Damage to these sensory structures can result from various factors, including sound overexposure, medications (e.g. aminoglycosides), disease, and age-related mechanisms, leading to auditory and vestibular deficits. Disorders can arise from this damage, causing hearing and balance problems that impact up to 15% and 20% of American adults, respectively (Blackwell et al., 2014; Neuhauser, 2016). While the loss of mechanosensory hair cells in the labyrinth has historically been considered the primary cause of inner ear dysfunction (Brosel et al., 2016; Yamasoba et al., 2013), recent evidence indicates that loss of ribbon synapses, coined a “synaptopathy,” can induce measurable deficits without accompanying hair cell loss.

Synapse loss oftentimes precedes hair cell loss in response to damaging auditory stimuli (Sergenyenko et al., 2013; Stamataki et al., 2006) impairing the transmission of sound. Auditory synaptopathies have been reported to contribute to temporary threshold shifts, deafness, and are linked to conditions such as hidden hearing loss and tinnitus (Hickox & Liberman, 2014; Kujawa & Liberman, 2009; Sergenyenko et al., 2013; Vasilkov et al., 2023; Viana et al., 2015; Wu et al., 2019).

In contrast to the cochlea, limited evidence of a symptomatic decline in synapse density exists in the vestibular periphery. Synaptic dysfunction has been hypothesized as a potential mechanism underlying spontaneous vertiginous disorders such as vestibular neuritis (Rauch, 2001), ischemic vertigo (Halmagyi et al., 2010), and Meniere's disease (Foster & Breeze, 2013), but reliable models and analyses are absent from the literature. Reductions in synapse density have been correlated with behavioral and functional impairments of the vestibular periphery in experimental rodent models of the aging-utricle (Wan et al., 2019) and after induction of excitotoxic lesions (Cassel et al., 2019). These findings suggest that vestibular synaptopathies contribute to the development of measurable dysfunction in animals.

Plasticity of vestibular synapses has also been reported within the murine maculae following spaceflight. Increases in ribbon synapse density within both type I and type II hair cells were reported in the rat utricle (Ross 1994, 2000), while decreases in synapse density within the extrastriola of the mouse utricle (Sultemeier et al., 2017) were reported following microgravity exposure. Interestingly, a decrease in utricular function proportional to the synapse loss reported in Sultemeier et al., 2017 has been reported in cosmonauts immediately upon their return to Earth's gravity, with gradual recovery over a 30-day period (Hallgren et al., 2016). With evidence supporting the hypothesis that alterations of synapses within the vestibular epithelia cause the development of measurable and symptomatic dysfunction, it is critical to investigate the synaptology of the vestibular periphery.

Due to the various mechanisms by which synapses of the inner ear may be altered and the potential downstream effects of these modifications, identification of synaptic ribbons and postsynaptic structures remains a vital step in the analysis of audiovestibular pathology. Electron microscopy (EM) is a reliable method for visualization of synaptic ribbons and their respect afferents, but due to its low sampling capabilities, immunofluorescence paired with confocal microscopy has arisen as a more efficient method of synapse quantification. Ribbons can be identified using antibodies raised against C-terminal binding protein 2 (CtBP2), a transcription factor that is a crucial element of the synaptic ribbon within the sensory systems (Schmitz et al., 2000). Use of immunofluorescence for ribbon analysis poses challenges such as labeling of nuclear CtBP2 and a lack of specific criteria to classify CtBP2+ puncta as a component of a synapse. As a result, identification of synaptic ribbons and their associations with a postsynaptic marker have become common in studies within the inner ear.

Markers of postsynaptic complexes have been implemented as valuable tools to investigate potential modifications of synaptic ribbons and their respective afferents. Postsynaptic markers may label neuronal structures such as auditory nerve terminals, calyces and boutons, or glutamatergic receptors indicating that a ribbon is in proximity to an afferent structure. The calyx that envelops type I hair cells is a large dendritic structure that can be visualized with immunofluorescence utilizing antibodies raised against neuron-specific structural filaments (e.g. β-III tubulin, neurofilament) (Fernandez et al., 1988; 1990). The labeling of these structures facilitates the identification of hair cell phenotypes in vestibular tissues. Type II hair cells, however, are not enveloped by a large afferent structure, rather they are innervated by multiple fine bouton projections (Fernandez et al., 1988; 1990) which are rarely sufficiently labeled to capture with confocal microscopy. To ensure ribbons within type II hair cells can be accurately accounted for, markers of a glutamatergic postsynaptic density can be added during the immunofluorescence protocol.

In the cochlea, postsynaptic markers have included the AMPA receptor subunit GluR2 (Liberman et al., 2011; Martinez-Monedero et al., 2016), postsynaptic density protein 95 (PSD-95) (Braude et al., 2015; Davies et al., 2011), and scaffolding proteins Shank1a (Braude et al., 2015) and Homer1 (Hosoya et al., 2021). GluR2 is one of the most commonly used postsynaptic markers in the cochlea, as cochlear ribbons have been reported to have high rates of association with the receptor subunit, with approximately ~97% of CtBP2+ puncta juxtaposed with a GluR2+ punctum (Martinez- Monedero et al., 2016). With such high cochlear associations, it is a logical assumption that GluR2 may be a pan-marker for postsynaptic complexes throughout the inner ear.

Despite its success in the cochlea, studies within the vestibular epithelia provide a significant contrast between vestibular and cochlear synaptic architecture. Within vestibular hair cells, ribbons do not appear to follow the patterns observed in the cochlea as less than 50% of vestibular ribbons were reported to be located within 1 μm of a GluR2/3+ punctum (Cassel et al., 2019; Gomez-Casati et al., 2010, Sadeghi et al, 2014). Other postsynaptic markers have been used in studies of vestibular ribbon synapses such as Shank1a (Sultemeier et al., 2017) and Homer1 (Wan et al., 2019), yet there is no consensus on how to count synapses with methods differing from study to study. The lack of empirical criteria and the frequent manual segmentation of synapses make it difficult to interpret results and derive conclusions from combined data across multiple studies.

Given the potential consequences associated with synaptic dysfunction, quantification of these synapses is crucial for understanding the translational impacts of changes in synaptic ribbon distributions. To provide unbiased conclusions about the effects of synaptopathies on audiovestibular function, methods must be refined and strategies rigorously evaluated. In order to optimize synapse quantification and capture the accurate amount of ribbon associations, the use of two postsynaptic markers, β-III tubulin and another postsynaptic density marker such as Homer1, can be implemented. The use of both an afferent and a postsynaptic density marker

reflects the most accurate number of synaptic connections, allowing for the quantification of large amounts of ribbons, encompassing those within both hair cell phenotypes within the vestibular periphery.

This study aims to introduce a strategy for synapse quantification through (1) establishing criteria to determine CtBP2+ puncta as the presynaptic component of a ribbon synapse, (2) optimizing the capture of ribbon synapses within each hair cell phenotype for a more accurate representation of synapse distributions with more comprehensive postsynaptic labeling, and (3) employing semiautomated analysis of large regions of inner ear tissue to minimize bias from manual synapse segmentation, accelerating research on synaptic dysfunction within the inner ear.

METHODS

Specimen Harvesting:

Labyrinths from 8-12 week old wild-type C57Bl/6J mice were harvested for the present study. 4% paraformaldehyde diluted in 0.1 M phosphate buffered saline (pH 7.4) was infused into the vestibule via an opening created within the bony labyrinth posterior to the cochlear nerve. The membranous labyrinth was perforated to identify the utricle then fixative perfused into the vestibule to remove the otolithic membrane. The entire temporal bone was then placed in fixative for 2h. After fixation, the temporal bones were thoroughly rinsed using 0.1 M PBS then placed in a 30% sucrose solution until the epithelia were harvested. Once harvested, intact epithelia were placed into 30% sucrose solution overnight as a cryoprotective measure. Utriculi were then embedded in Optimal Cutting Temperature compound (O.C.T., PANTek Technologies LLC #23-730-571) and allowed to freeze until solid.

Immunohistochemical Processing:

Utriculi were cryosectioned at 15 µM and immediately mounted onto Superfrost™ Plus Microscope slides (12-550-15, Thermo Fisher Scientific) and stored at –20°C overnight. Adjacent sections were incubated in blocking solution (1.0% Triton X-100, 10% normal donkey serum solution in PBS) overnight at room temperature in a primary antibody cocktail including anti-CtBP2 (1:250; mouse anti-CtBP2), either anti-Homer1 (1:250; guinea pig anti-Homer1) or anti-GluR2 (1:250, guinea pig anti-GluR2), anti-β-III Tubulin (1:250, rabbit anti-β-III Tubulin), and anti-calretinin (CALB2) (1:250, chicken anti-CALB2) in blocking solution (see Table 1 for antibody information). At the conclusion of primary antibody incubation, specimens were washed in 0.1 M PBS (3 times for 10 min). Sections were then incubated for 2 hours at room temperature in secondary antibodies diluted in blocking solution that included Alexa Fluor 594-conjugated donkey anti-mouse IgG antibody (1:250; A32744; Thermo Fisher Scientific), Alexa Fluor 488-conjugated donkey anti-rabbit IgG antibody (1:250; A32790; Thermo Fisher Scientific), STAR RED-conjugated donkey anti-guinea pig (1:200, Abberior Instruments), and Alexa Fluor 405-conjugated donkey anti-chicken IgY (IgG) antibody (1:250; 703-475-155; Jackson ImmunoResearch Laboratories). Liquid silicone antifade mounting medium was applied then coverslips placed atop the section, then sealed with clear nail polish.

STED Imaging & Image Analysis:

Specimens were imaged using a 60X objective (Olympus silicone-immersion objective N.A. 1.3) on a Facility Line Stimulated Emission Depletion (STED) confocal microscope (Abberior Instruments, Bethesda, MD). Image stacks (35 µm X 35 µm (XY), 438 px x 438 px (XY)) were acquired from the striola, medial extrastriola, and lateral extrastriola of each utricle using the presence of CALB2+ calyces to identify the striola (Desai et al., 2005; Hoffman et al., 2018). The raw image stacks were subsequently deconvolved using Huygens Deconvolution software (Scientific Volume Imaging Inc.) and analyzed with custom MATLAB scripts developed in the laboratory. The image analysis software enabled automated detection and segmentation

of CtBP2+, GluR2+, and Homer1+ puncta, as well as segmentation of TUBB3+ calyces, boutons, and parent axons. Additionally, CtBP2+ puncta within the inner face of the calyx (synapses within type I hair cells) were distinguished from those outside the labeled calyces (synapses within type II hair cells).

Synapse Quantification

A graphic summarizing the synapse quantification workflow can be followed in Figure 1. Condensing these steps into an easily visualized graphic aids in understanding the workflow described within the methods.

Intensity-Based Clustering Segmentation and 3D Object Recreation

Deconvolved image stacks were uploaded into MATLAB as raw TIFF files. A K-Means clustering intensity-based segmentation was applied to each stack to isolate putative puncta from background labeling. This clustering method delineates aggregates of post-threshold CtBP2+ puncta (putative ribbons) from potential background labeling. Seed points were identified in the first optical section of the image stack where each object appears, and an active contour was applied to reconstruct putative ribbons in three dimensions. An active contour algorithm is an iterative, region growing algorithm that reforms objects split between adjacent optical sections to create 3D renderings of how they would reside in the epithelia. (MATLAB, MathWorks Inc., 2024).

β-III tubulin labeling tends to become fragmented during confocal microscopy and image deconvolution due to labeling of fine microtubules. As a result, the channel for β-III tubulin undergoes a similar analysis with similar region growing and fiber dilation algorithm applied to ensure the labeling of calyces was not fragmented by the image analysis pipeline. A Wiener filter was applied to reduce signal-to-noise while preserving β-III tubulin labeling within the calyx, removing spurious labeling sometimes produced with image thresholding. The combination of

an active contour with a Wiener filter accurately reconstructs calyces in 3D with minimal fragmentation allowing for enhanced confidence in distance analyses.

Based on previous data obtained from 3D EM stacks and recreations of ribbons, it was determined that it would be unlikely to encounter a ribbon with a diameter < 100 nm, as nothing in the data was observed to be that small. Compiling this information with previously obtained volumes of immunolabeled ribbon volumes, a size filter (sphere-like objects with a radius ≤ 0.037 μm and volume ≤ 3 voxels in volume) was applied to remove out labeling in the cell nuclei as well as any potential background. All remaining objects with a volume greater than 3 voxels within the CtBP2 active contour were assigned an ID to extract pertinent information such as volume, centroid, associated hair cell phenotype, and distance from postsynaptic markers.

Ribbon Associations with Postsynaptic Markers

Once the active contours for each channel were completed, distance calculations from each ribbon object to Homer1, GluR2, and β-III tubulin objects were performed. To determine the distance between a CtBP2+ puncta and a GluR2/Homer1+ puncta, a surface-to-surface Euclidean distance was calculated from each CtBP2+ object to the nearest GluR2+ or Homer1+ puncta in the stack. Ribbon objects were considered closely apposed to GluR2/Homer1 if they fell within a 0.3 μm threshold. Within a previous data set of immunolabeled stacks with postsynaptic markers, the Euclidean distance from ribbon objects to postsynaptic markers was calculated. The 0.3 μm distance threshold was empirically determined using a probability density function, where the likelihood of any distance larger than that would be unlikely when using super-resolution microscopy. As STED microscopy provides a resolution down to 80 nm, it is believed that this distance threshold is accurate with the imaging parameters described. A similar approach was taken to analyze associations with β-III tubulin. Due to the heterogeneity in ribbon volumes, first a centroid-to-centroid distance calculation was applied for CtBP2- β-III tubulin associations. Larger ribbons can be lost due to this filter due to larger diameters; thus

centroid-to-centroid distances are unable to determine accurate associations for this subset of ribbons. To prevent the potential loss of larger ribbons, all objects that failed the centroid-to-centroid distance filter underwent a subsequent surface-to-centroid calculation, measured from the surface of the ribbon to the centroid of the nearest β-III tubulin object. All putative ribbon objects that fell within the 0.3 μm distance threshold were considered associated with the postsynaptic marker.

Type I vs. Type II Ribbon Determination

To distinguish ribbons within the calyx of a type I hair cell from ribbons within type II hair cells, semiautomated segmentation of calyces was performed using the Volume Segmenter Application (MATLAB, MathWorks Inc., 2024). The β-III tubulin active contour was loaded into the application and the inner face of each calyx object was outlined without segmenting the tubulin labeling. Labeling began at the first appearance of a calyx outline, assigning it a unique label. Segmentation then occurred every four to five optical sections then was auto interpolated through the stack, removing the need for manual segmentation of each optical section. These labels were then loaded into the specialized MATLAB script to differentiate objects within a type I hair cell type II hair cells (lateral face projections and boutons).

Statistical Analyses

As a result of how the data for each analysis were collected, different statistical tests were deemed appropriate dependent on the subset of data analyzed. To compare GluR2 associations across the topology, a repeated measures ANOVA was implemented as the sample sizes were equal, the data appeared to be normally distributed, but image stacks from different regions of the same animals were compared, requiring the inclusion of a repeated measures test. Determining differences in Homer1 associations across the topology required a non-parametric repeated measures ANOVA due to differences in how the image stacks were

obtained and overlap between the animals used. Friedman's test, a non-parametric equivalent of the repeated measures ANOVA was used to determine potential differences between the different regions. Overlap existed between some animals used to determine Homer1 and GluR2 associations. To address the overlap and the failure to adhere to the assumptions of parametric and non-parametric ANOVAs, a linear mixed-effects model was implemented, then an ANOVA performed to determine differences in ribbon association with either postsynaptic marker.

Ribbon volumes across the topology were combined as raw volume values (in μm^3) extracted from MATLAB, giving three different groups of accrued data, that did not meet the assumptions of parametric testing. As a result, a Kruskal-Wallis test was performed on the data to determine differences across the utricular topology. These differences were further investigated by using a Dunn-Holland Wolfe test, a non-parametric multiple comparison test. A similar approach was taken to calculate differences in volumes between ribbons within type I hair cells and type II hair cells, using the Kruskal-Wallis test, which is the equivalent to a Mann-Whitney U test for two groups.

RESULTS:

CtBP2 Association with GluR2

Due to its use within the cochlea and previous uses within the vestibular periphery, the association between CtBP2 and GluR2 was examined to evaluate its role as a potential postsynaptic marker in the utricle (Liberman et al., 2011; Martinez-Monedero et al., 2016; Sadeghi et al., 2014). Synaptic ribbon association with the AMPA receptor subunit GluR2 was consistently observed to be under 40% across the various regions of the utricle, consistent with previous studies (Fig. 4) (Cassel et al., 2019; Gomez-Casati et al., 2010, Sadeghi et al, 2014). Compiled results for associations of the synaptic ribbon with the different postsynaptic markers can be visualized in Table 2.

In the striola, 31.5 ± 4.2% of ribbons were found to be associated with GluR2. 35.8 ± 5.6% of ribbons within the medial extrastriola and 34.7 ± 2.5% within the lateral extrastriola were observed to be closely apposed with GluR2 (Fig. 4C). No differences in CtBP2 association with GluR2 were observed between the topological regions of the utricle (Repeated measures ANOVA, $p = 0.82$). 85.2 ± 7.6% of synaptic ribbons were apposed to β-III tubulin in the striola, while 78.6 ± 4.6% of ribbons within the medial extrastriola and 81.4 ± 2.7% of ribbons within lateral extrastriola were found to be apposed (Table 2). When the number of ribbons captured by both GluR2 and β-III tubulin were combined, associations increased to: 87.9 ± 8.0 % in the striola, 83.8 ± 5.3% in the medial extrastriola, and 85.5 ± 2.6% in the lateral extrastriola (Fig. 4C).

Of the total number of ribbons within type I hair cells captured within the striola, 35.6 ± 3.9% were classified as associated with GluR2, while 35.9 ± 12.6% of ribbons within type II hair cells were associated with GluR2. Within the medial extrastriola, 45.2 ± 2.9% of ribbons within type I hair cells were associated with GluR2, while 39.9 ± 6.8% of ribbons within type II hair cells were associated with GluR2. In the lateral extrastriola, 44.3% ± 2.5% of ribbons within type I hair cells were associated with GluR2 and 39.3 ± 3.3% of ribbons within type II hair cells were associated with GluR2 (Table 2, Fig. 4D). No differences were observed with ribbon association with GluR2 between type I and type II hair cells across the topology (Repeated measured ANOVA, $p = 0.18$). These combined data suggest that GluR2 alone is not a robust marker for synaptic ribbons, but addition of β-III tubulin provides critical information about the afferent associations of the ribbons.

CtBP2 Association with HOMER1

As the reported and observed association of synaptic ribbons with GluR2 was found to be lower in the vestibular periphery compared to the cochlea, Homer1, an alternative postsynaptic density marker previously used within the cochlea and vestibular epithelia, was

labeled in conjunction with β-III tubulin (Hosoya et al., 2021; Wan et al., 2019). No differences were observed in the association of CtBP2+ puncta with Homer1+ puncta across the various regions of the utricle (Friedman's Test, $p = 0.72$). A compiled form of the reported data displaying ribbon associations with each postsynaptic marker and phenotype can be seen in Table 3.

Within the striola, 63.4 ± 6.9% of synaptic ribbons were found to be associated with Homer1, 75.7 ± 5.4% of ribbons were closely apposed to β-III tubulin, capturing a total of 87.2 ± 7.7% of ribbons within the striola. The ribbons within the medial extrastriola exhibited a Homer1 association 60.1 ± 4.3%, 75.0 ± 3% close apposition to β-III tubulin, capturing a total of 87.7 ± 4.3% of synaptic ribbons in this region. In the lateral extrastriola, 62.0 ± 2.5% of ribbons were closely apposed to Homer1, while 81.6 ± 1.9% were in close apposition to β-III tubulin. A combination of both markers yielded a total capture of 89.3 ± 2.1% of ribbons within the lateral extrastriola. These findings indicate that there is a general consistency in the association of synaptic ribbons with Homer1 across different regions of the utricle.

Similar to phenotypical associations with GluR2, no differences were observed between Homer1 associations of ribbons within type I hair cells and type II hair cells (Friedman's Test, $p = 0.08$). Of the total number of ribbons within type I hair cells captured within the striola, 65.3 ± 7.0% and 77.4 ± 8.9% of ribbons within type II hair cells were associated with Homer1. Within the medial extrastriola, 64.8 ± 4.0% of ribbons within type I hair cells were associated with Homer1 and 72.3 ± 2.9% of type II ribbons were associated with Homer1 (Figure 5D). In the lateral extrastriola, 59.2 ± 5.0% of ribbons within type I hair cells and 70.2 ± 6.0% of those within type II hair cells were associated with Homer1. The similar association of Homer1 with type I and type II hair cells highlights a similar synaptic composition of vestibular ribbon synapses across the topology, which could have implications for understanding the functional diversity of synaptic distributions within the utricle.

Homer1 vs. GluR2 Association

As the data suggested potential differences of ribbon association with GluR2 and Homer1, results were compared between the analyzed specimens. To test the hypothesis that there are no differences in ribbon associations with GluR2 and Homer1, a linear mixed-effects model was employed and an ANOVA performed on the compiled data. When compared to GluR2, more ribbons were found to be associated with Homer1 across the topology of the utricle (linear mixed-effects model ANOVA, $F = 19.13$, $p = 0.01$), rejecting the null hypothesis. These data indicate higher associations with Homer1 across the utricular topology and are consistent with previous studies using GluR2 within the vestibular periphery. Potential implications of these associations are postulated in the Discussion.

Ribbon Volumes Vary Across the Topology of the Utricle

Within the cochlea, differences in ribbon volumes exist at the basolateral membrane of inner hair cells. Smaller ribbons were reported to be localized on the modiolar face of the hair cell while larger ribbons were found at the more on the pillar face of the hair cell (Liberman et al. 2011). These differences in ribbon sizes suggest a potential functional contribution of ribbon size in relation to afferent properties within the auditory periphery.

Within the maculae, afferent firing rates are correlated to their topological innervation pattern, either within the striola or extrastriola (Goldberg et al., 1990a). Previous studies using EM obtained stacks of ribbons from striolar type I hair cells and extrastriolar type I hair cells reported no differences in ribbon volumes across the topology (Michanski et al. 2023), yet only few ribbons from each region were analyzed. To investigate potential topological contributions to difference in ribbon volume, volumes of ribbons were compared across the three regions of the utricle—the striola, medial extrastriola, and lateral extrastriola. Differences in ribbon volumes were observed between the different topological regions of the utricle (Fig. 6A) (Kruskal-Wallis test, $H_0 = 20.80$, $H_{crit} = 13.81$, $p < 0.001$). Within the striola, ribbon volumes were found to be

larger than ribbons in both the medial extrastriola (Non-parametric multiple comparison test, Dunn-Holland Wolfe, $Q_t = 4.30$, $Q_c = 3.59$, $p < 0.001$) and the lateral extrastriola (Non-parametric multiple comparison test, Dunn-Holland Wolfe, $Q_t = 3.77$, $Q_c = 3.59$, $p < 0.001$).

Ribbon Volume by Hair Cell Phenotype

While the physiology of vestibular hair cells has been studied extensively, phenotype-dependent distinctions between ribbons within type I hair cells and type II hair cells have not been widely reported. Recent studies have indicated ribbon volumes differences between type I and type II hair cells (Michanski et al. 2023) suggesting a potential correlation between hair cell phenotype and ribbon volume. To test the hypothesis that hair cell phenotype has no influence on ribbon volume, captured ribbon volumes from those within type I and type II hair cells were differentiated using this quantification algorithm. In contrast to the published literature, no difference in ribbon volumes was observed between ribbons within type I hair cells and within type II hair cells, suggesting hair cell phenotype does not influence the volume of the ribbon (Fig. 6B) (Kruskal-Wallis test, $H_0 = 0.23$, $H_{crit} = 0.63$, $p > 0.05$).

DISCUSSION:

Use of Homer1 Allows for Increased Capture of Vestibular Ribbon Synapses

This study aligns with the findings of previous studies, where less than 50% of CtBP2+ puncta were found to be within 1 µm of GluR2/3+ puncta in the rat crista, as less than 40% of ribbons were found to be within 0.3 µm of GluR2. Homer1 associations provide a clear contrast to the available literature with an average of 62% of ribbons associated with the marker across the utricular topology. Sadeghi et al. 2014 reported an increased association of ribbons within type II hair cells with GluR2, No differences were determined between ribbon associations with GluR2 or Homer1 based on hair cell phenotype, conflicting with the findings of Sadeghi et al., 2014. It is possible that the differences in these studies could be due to the use of a smaller

distance filter and super-resolution imaging techniques used in this study. Potential differences in GluR2 distributions may also exist between mouse and rat vestibular epithelia.

The lack of GluR2 association with higher Homer1 association indicates the likelihood of a different distribution of glutamatergic receptors within the vestibular periphery than what was previously reported. This theory is further supported by the observation that many synaptic ribbons lack association with either Homer1 or GluR2 yet are still associated with β-III tubulin. The likely presence of these alternative receptor subunits could suggest a more complex distribution of AMPA receptor subunits (GluR1,3,4) within vestibular afferents. It could also signify a potential contribution of NMDA or mGluR receptors within the vestibular periphery, although the slower kinetics of these receptors make their involvement in the rapid transduction of vestibular stimuli unlikely.

The culmination of these findings reveals a much deeper complexity to vestibular synaptology, calling for a broader investigation into the molecular architecture of synapses in the vestibular epithelia, with the intent to map out the full spectrum of receptor associations and distributions. Understanding the specific roles and interactions of these glutamate receptors, along with their relation to afferent physiology, could provide crucial insights into the mechanisms of synaptic transmission and plasticity within the vestibular periphery, leading to a new method of evaluating vestibular dysfunction at the synaptic level and lay the framework for future therapeutic interventions.

Significance of Homer1 at the Vestibular Ribbon Synapse

The associations involving Homer1 are of particular interest, as existing literature indicates that synapses within the maculae retain the potential for plasticity in response to changes in ambient gravity (Ross 1994, 2000; Sultemeier et al., 2017). Homer1 has been implicated in the plasticity of synapses within the central nervous system (Tu et al., 1998; Xiao et al., 1998; Yoon et al., 2021), which may account for its association with peripheral synapses

within the labyrinth. Given Homer1's involvement with metabotropic glutamate receptors (mGluRs) and the limited evidence regarding the roles of mGluRs within the labyrinth, it is plausible that these receptors may play a larger role in the vestibular periphery than once thought. Metabotropic glutamate receptors have been described in the cochlea (Klotz et al., 2019) and within hair cells of the frog cristae and maculae (Guth et al., 1998), yet not on the afferents themselves.

The presence of Homer1 at many postsynaptic densities suggests a critical role in synaptic development and regulation within the inner ear. Homer1's association with synaptic plasticity in the CNS highlights its potential significance in activity-dependent plasticity within the vestibular maculae. Understanding this relationship could provide new insights into how synaptic architecture adapts to environmental changes, particularly in gravity-dependent contexts. In summary, the study of Homer1 associations within the vestibular system opens a promising avenue for understanding the synaptology of the vestibular epithelia. Further research in this area could significantly enhance our knowledge of vestibular function and its adaptation to changes, contributing to the development of targeted therapeutic strategies for vestibular disorders.

Potential Contributions of Large Striolar Ribbons

As previously stated, cochlear ribbons vary in size dependent upon their location on the basolateral membrane within the inner hair cell. Their sizes followed a gradient across the hair cell with smaller ribbons found to be associated with low-threshold fibers on the modiolar face becoming progressively larger across the hair cell with larger ribbons associated with medium- and high-threshold fibers on the pillar face (Liberman et al. 2011). The difference of size may be explained due to the higher thresholds of afferents along the medial and modiolar face of the hair cell which could require a more substantial release of glutamatergic vesicles to fire an action potential.

While differences of individual fibers innervating hair cells have not been reported on the same scale as auditory nerve fibers, afferents within the vestibular epithelia possess topology dependent physiologic responses. Afferents innervating the extrastriola exhibit tonic responses with sustained firing rates to a persistent stimulus such as gravity, proportional to otolithic membrane displacement. Striolar afferents exhibit a “tonic-phasic response” with a phasic burst of firing activity that adapts to a more tonic response over a short time period (Goldberg et al., 1990b). These unique physiological properties allow rapid responses encoding head movements in relation to gravity.

Larger ribbons within the striola could correlate with the physiology of the region, as phasic responses require a larger initial release of neurotransmitters when compared to tonic responses. Ribbons within the striola may have to be larger to meet the functional demands of the region, requiring the recruitment and release of large numbers of synaptic vesicles during dynamic head movements for accurate perception. Recent studies have reported larger ribbons within type I hair cells of the utricular striola, but not the extrastriola, of aging mice from image stacks obtained using transmission electron microscopy (TEM) (Michanski et al., 2023). It is difficult to draw comparisons between this study and Michanski et al. 2023, as the sampling capabilities of TEM are much lower than immunohistochemistry, so significantly fewer ribbons volumes were reported from far fewer hair cells. The volumetric data reported in this study was composed from thousands of ribbons sampled from hundreds of hair cells across the topology, making direct comparisons inefficient and inappropriate.

The significance of larger ribbons within the striola may also indicate an increased presence of ribbon “clusters” within the region. Ribbon clusters refer to multiple ribbons appearing to be aggregated together within the hair cell. Two distinctions can be made between these groups: clusters with one or more ribbons docked to the presynaptic membrane surrounded by “floating” or undocked ribbons, and clusters of ribbons that are not docked to the presynaptic membrane at all. Michanski et al., 2023 reported increases in ribbon clusters within

type I hair cells of the striola, but as a result of age rather than pathology. The use of super resolution confocal microscopy does not possess the capabilities to visualize compartmentalized ribbons within a cluster, so it is impossible to determine if the ribbons themselves were larger or more ribbon clusters were present within the striola in this study.

Lack of Phenotype-Dependent Differences in Ribbon Volumes

Recent literature has reported differences in hair cells dependent on hair cell phenotype, with type I utricular hair cells having larger ribbons than type II utricular hair cells at P18 (Michanski et al., 2023), yet the functional contributions of these findings remain unexplored. Changes in membrane capacitance (ΔC_m) were recently measured to be ten-fold higher in type II hair cells than in type I hair cells indicating a significantly higher exocytosis of synaptic vesicles from type II hair cells upon depolarization (Spaiardi et al., 2022), suggesting that ribbons within type II hair cells may be larger than those within type I hair cells. The results of this study conflict with these findings, however, as no volumetric differences between ribbons within type I hair cells and type II hair cells were observed across the topology of the utricle.

While the volumes of these ribbons were obtained from STED microscopy used to image immunofluorescent punctum, it would be logical to assume that larger punctum would represent clusters or larger ribbons, and these differences would be reflected in the data. The smaller exocytosis from type I ribbons may indicate a greater dependence on nonquantal transmission as a mechanism of synaptic transmission of type I hair cells to minimize the delays associated with quantal transmission as hypothesized in Govindaraju et al., 2023.

The inconclusive nature of these conflicting findings indicates the need for further studies to compare ribbon volumes captured with EM and immunofluorescence, paired with capacitance measurements to measure exocytosis from ribbons within both hair cell phenotypes across the topology.

Implementation of Semiautomated Synapse Analysis

The methodologies employed in this study offer a comprehensive and rigorous analysis of synaptic distributions across the topology of inner ear epithelia, with a particular emphasis on unbiased and empirical assessment of ribbon characteristics. By employing this semiautomated analysis, synaptic ribbons can be meticulously examined in three dimensions giving results in a timely matter without the need for analysis software and its associated script production and cost. This script enables the drawing of detailed and accurate conclusions regarding ribbon associations with postsynaptic markers, volumetric measurements, and phenotypic classifications across extensive regions of tissues.

The proposed synapse quantification script is highly adaptable, allowing for the modification of parameters to align with the settings of acquired image stacks and imaging resolution of the microscope. This analytical framework represents a significant advancement in the objective measurement of synaptic distributions under normal conditions or dysfunction, providing a reliable foundation for further research. Additionally, the ability to quickly analyze large regions enhances the efficiency and scope of the study, making it a valuable tool for researchers investigating the nuances of studying synapses within the inner ear.

CONCLUSION

In conclusion, the implementation of this advanced analytical technique not only provides objective and precise measures of synaptic distributions and ribbon characteristics but also opens new avenues for understanding the complex interplay between synaptic pathologies and clinical symptomatology. The use of this algorithm allows for a broad sampling of the various inner ear neuroepithelia, allowing for three-dimensional examination of image stacks, laying clear criteria for synapse quantification, and expediting analysis of ribbon synapses of the inner ear to significantly enhance the field’s understanding of audiovestibular synaptology. Acknowledging the potential inaccessibility of super-resolution microscopy, these parameters can be easily modified depending on the imaging capabilities of the confocal microscope used

as well, allowing for reliable synaptic analyses across the field. When these measurements are compiled with other physiological or anatomical methodologies, it can lead to profound conclusions about the impact of synaptic dysfunction on the development of clinical symptoms.

Table 1.

TARGET	HOST	MANUFACTURER	CATALOG NO.
CtBP2	Mouse	BD Bioscience	612044
Homer1	Guinea Pig	Synaptic Systems	160005
GluR2 (GluA2)	Guinea Pig	Synaptic Systems	182105
β-III Tubulin	Rabbit	BioLegend	802001
Calretinin (CALB2)	Chicken	Neuromics	CH22116

Table 1. Primary antibodies utilized in the present study. Antibodies were diluted in blocking solution at a concentration of 1:250, then applied to sections overnight to allow for optimal penetration.

Table 2.

	RIBBON ASSOCIATIONS				
Region	GluR2	β-III tubulin	GluR2/β-III tubulin	Type I + GluR2	Type II + GluR2
Striola	31.5 ± 4.2%	85.2 ± 7.6%	87.9 ± 8.0%	35.6 ± 3.9%	36.0 ± 12.6%
MES	35.8 ± 5.6%	78.6 ± 4.6%	83.8 ± 5.3%	45.2 ± 2.9%	39.9 ± 6.8%
LES	34.7 ± 2.5%	81.4 ± 2.7%	85.5 ± 2.6%	44.3 ± 2.4%	39.3 ± 3.3%
TOTAL	34.4 ± 3.7%	82.2 ± 2.0%	86.1 ± 1.7%	42.0 ± 1.1%	38.8 ± 1.8%

Table 2. Compiled data from specimens immunolabeled with CtBP2, GluR2, and β-III tubulin. Topological regions are broken down based on ribbon proximity to GluR2, β-III tubulin, and combined associations with ribbons closely apposed to either one of the markers (or both). Distinctions between ribbon apposition between those within type I and type II hair cells are displayed as well. No topological influence was observed on ribbon association with GluR2 observed between the different regions of the utricle (Repeated measures ANOVA, $p = 0.82$), as well as no phenotypical influence on the association of type I ribbons and type II ribbons with GluR2 (Repeated measures ANOVA, $p = 0.18$).

Table 3.

	RIBBON ASSOCIATIONS				
Region	Homer1	β-III tubulin	Homer1/β-III tubulin	Type I + Homer1	Type II + Homer1
Striola	63.4 ± 6.9%	75.7 ± 5.4%	87.2 ± 7.7%	65.3 ± 7.0%	77.4 ± 8.9%
MES	60.1 ± 4.3%	75.0 ± 3.0%	87.7 ± 4.3%	59.2 ± 5.0%	70.2 ± 6.0%
LES	62.0 ± 2.5%	81.6 ± 1.9%	89.3 ± 2.1%	64.7 ± 4.0%	72.3 ± 2.9%
TOTAL	61.8 ± 1.5%	77.4 ± 1.2%	88.1 ± 1.6%	63.5 ± 1.9%	73.1 ± 2.0%

Table 3. Compiled data from specimens immunolabeled with CtBP2, Homer1 and β-III tubulin. Associations are broken down by topological location as well as proximity to Homer1, β-III tubulin, and combined associations with ribbons closely apposed to either one of the markers. Distinctions between ribbon apposition with Homer1 between those within type I and type II hair cells are reported as well. No topological influence was observed on ribbon association with Homer1 across the different regions of the utricle (Friedman's Test, $p = 0.72$), as well as no phenotypical influence on the association with Homer1 (Friedman's Test, $p = 0.08$).

Figure 1.

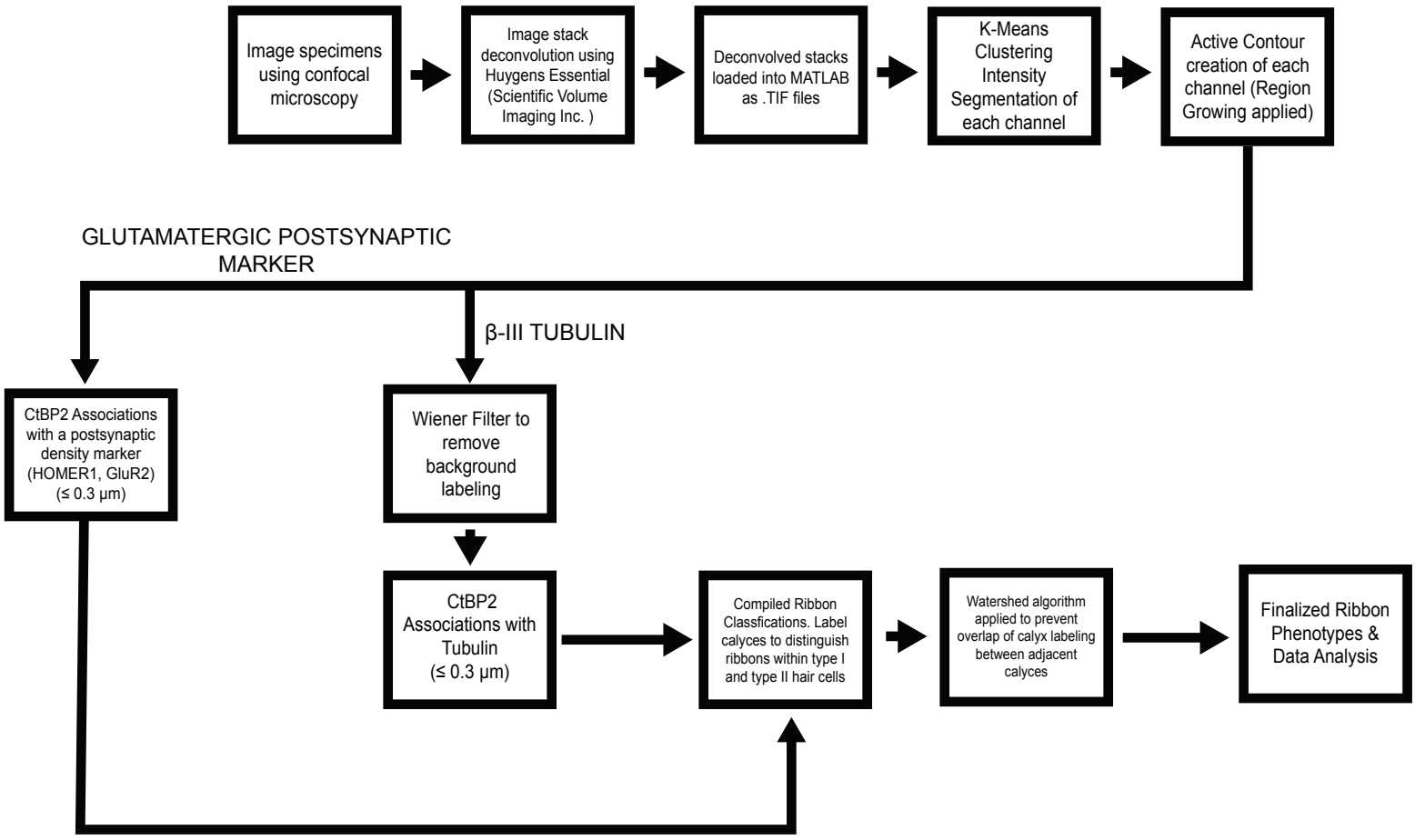

Figure 1. Flow chart describing the various steps of the image analysis pipeline used to analyze the data reported in this thesis. Image stacks can be obtained using any confocal microscope, as the parameters of the scripts are able to be modified. The image stacks in this study were obtained using STED microscopy with 80 nm X 80 nm X 80 nm voxels in 35 μm X 35 μm regions. Stacks were further processed using Huygens Essential deconvolution software (Scientific Volume Imaging Inc.) using the same parameters for each specimen. Post-deconvolution, stacks were uploaded into MATLAB (MathWorks Inc.) as .TIF files. Once uploaded, each stack underwent a K-means clustering intensity based segmentation. This segmentation allowed for seed points to be plotted for each ribbon, from which a region growing (activecontour) algorithm was implemented to recreate labeling in each channel into binary objects. Ribbons less than 3 voxels in volume were excluded as they are likely nuclear labeling. A Wiener filter was then applied to the β-III tubulin channel to remove residual background labeling. After completion of the active contour, ribbons were given a unique ID number and associations between the glutamatergic postsynaptic density marker (i.e. GluR2, Homer1) and β-III tubulin were calculated. For GluR2/Homer1 associations, surface-to-surface Euclidean distances were calculated from each ribbon object to each object. If a ribbon was within 0.3 μm of a PSM object, it was considered to be closely apposed/associated. For β-III tubulin associations, centroid-to-centroid distances were calculated, with the same distance threshold. Due to the presence of larger ribbons with larger diameters, if a ribbon failed the centroid-to-centroid distance threshold, a surface-to-centroid measurement was calculated. Segmentation of calyces was performed in the Volume Segmenter Application in MATLAB, with labeling beginning at the first appearance of a distinct calyx-like object, and repeated every four-five optical sections until it was no longer discernable. Labels were autointerpolated down the stack to create a void within each calyx. A Watershed algorithm was then applied to prevent overlap of calyx labeling, then phenotype assignment of ribbons was automatically determined using the labels.

Figure 2.

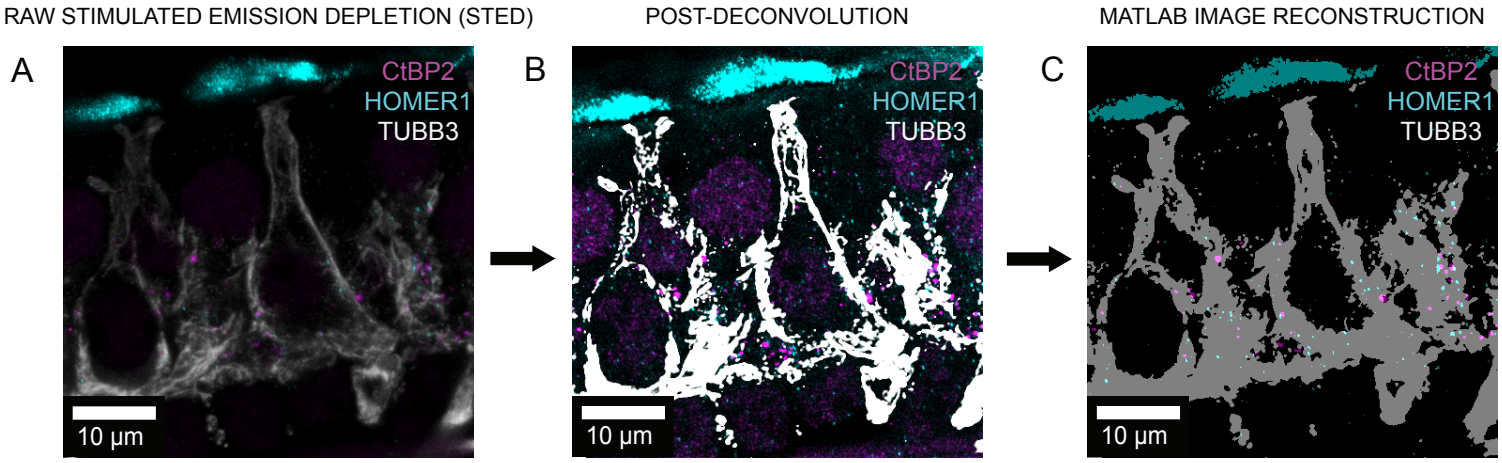

Figure 2. Image Analysis Pipeline. (A) An optical section derived from a raw z-stack acquired using Stimulated Emission Depletion (STED) microscopy. The application of STED microscopy reduces the distortion commonly observed with conventional light microscopy. CtBP2 (magenta) is observed associated with various Homer1 (cyan) puncta, as well as calyces enveloping type I hair cells (TUBB3, white/gray). (B) The same optical section as in (A), post-deconvolution. Deconvolution is employed to further reduce optical distortions inherent in light microscopy. These images are representative of the stacks used to reconstruct objects shown in (C). (C) The output of the laboratory's semi-automated synapse quantification script in MATLAB. Objects are reconstructed using an active contour to accurately define objects in (A) and (B), providing precise synapse densities and volumetric measurements. This optical section is representative of the data used for ribbon quantification.

Figure 3.

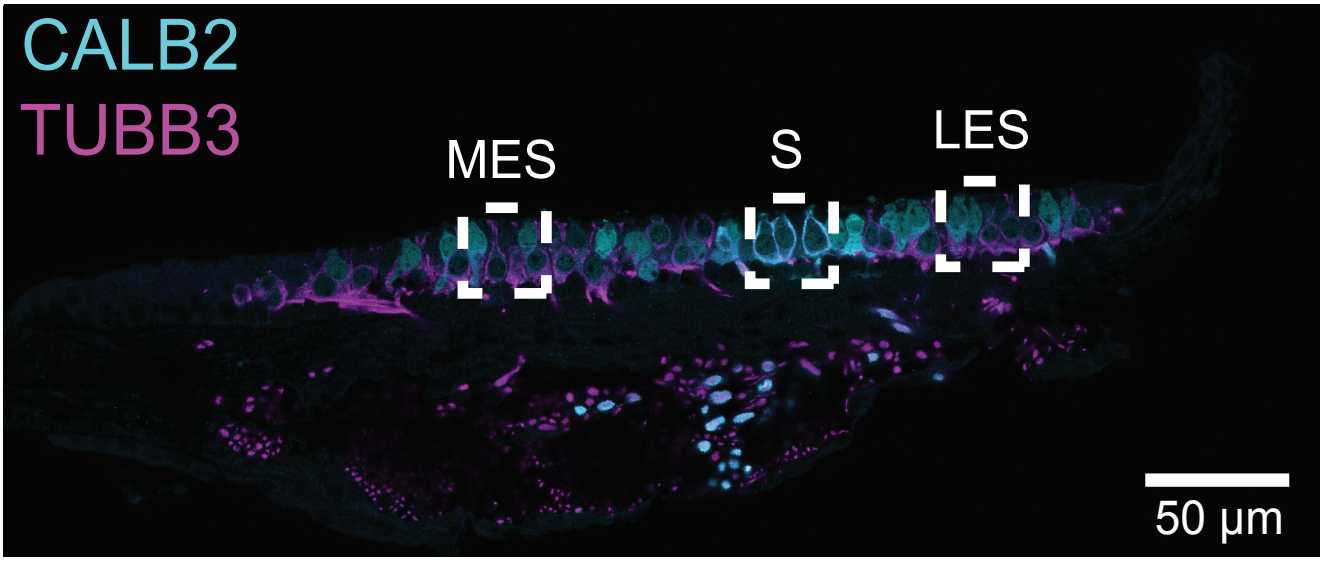

Figure 3. Low power micrograph depicting the topology of the murine utricle. The striola (S) was identified using calretinin (CALB2, cyan) to identify calyces within the striola (Desai et al., 2005) from calyces of the lateral and media extrastriola (TUBB3, magenta). The extrastriolar regions, lateral (LES) and medial (MES) were identified based on anatomical positions and size of the region. Sections were 15 µm thick, allowing for broad sampling across the utricle. Dashed boxes represent the approximate XY dimensions of the obtained image stacks for each region (35 µm x 35 µm).

Figure 4.

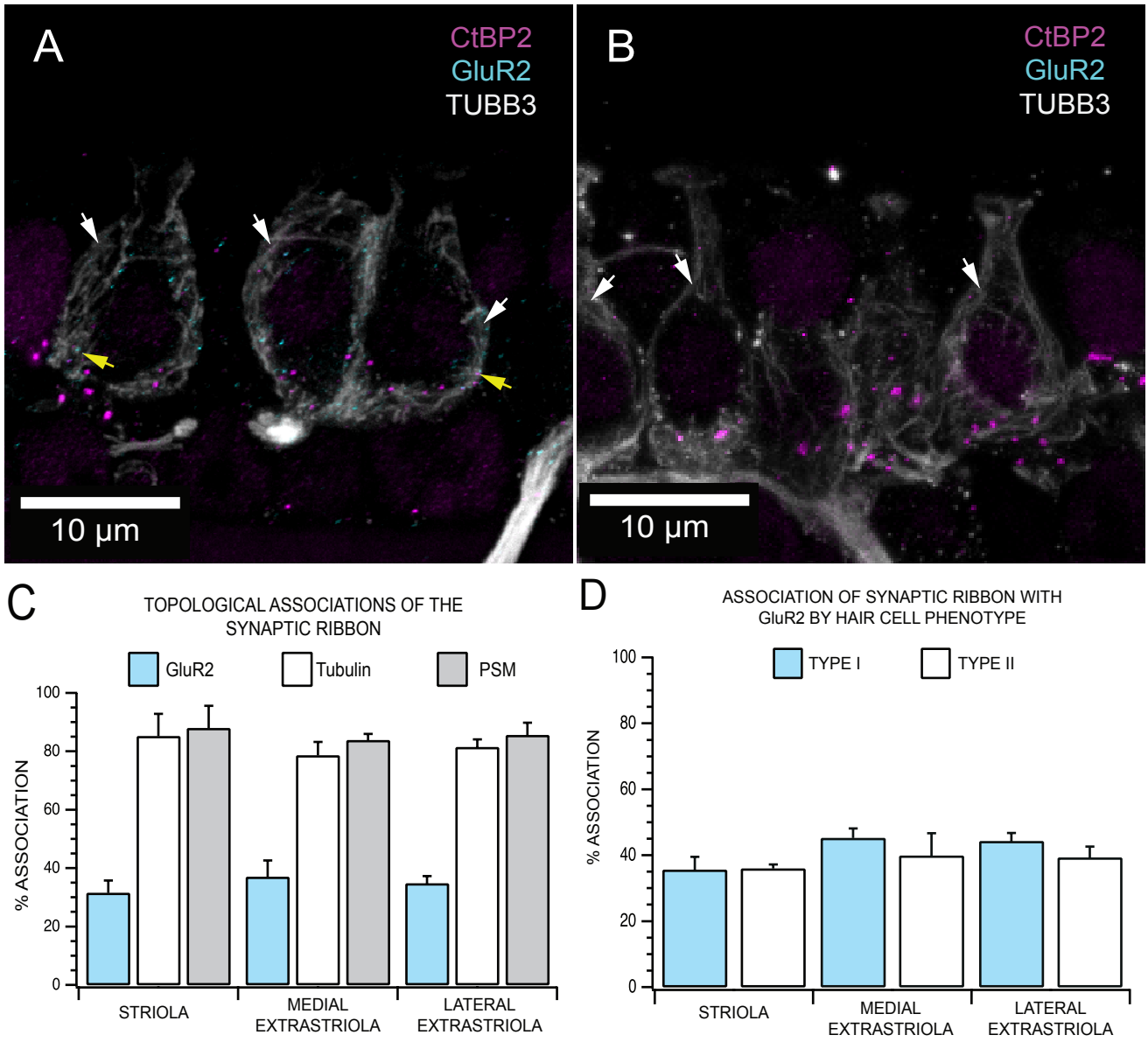

Figure 4. (A) Maximum intensity projection of a substack of optical sections from the striola of a mouse utricle using obtained using STED microscopy. The calyces enveloping type I hair cells (white arrowheads) can be visualized using antibodies raised against β-III tubulin (white). CtBP2 (magenta) appears to have a poor colocalization with the AMPA receptor subunit GluR2 (cyan, yellow arrowheads). GluR2 labeling can be visualized on the inner and outer face of the calyx, as well as at the base of Type II hair cells. (B) Maximum intensity projection of a substack of optical sections used as a no primary control for GluR2. No labeling was observed in the channel for GluR2, confirming antibody specificity. (C) Topological breakdown of GluR2 associations across the utricle. Error bars represent the standard deviation. PSM (postsynaptic marker) indicates association with either GluR2, β-III tubulin, or both. No differences in ribbon association with GluR2 were observed between the different topological regions of the utricle (Repeated measures ANOVA, $p = 0.82$). (D) Breakdown of ribbon associations with GluR2 based on hair cell phenotype. No differences were found between the association of type I ribbons and type II ribbons with GluR2 (Repeated measures ANOVA, $p = 0.18$).

Figure 5.

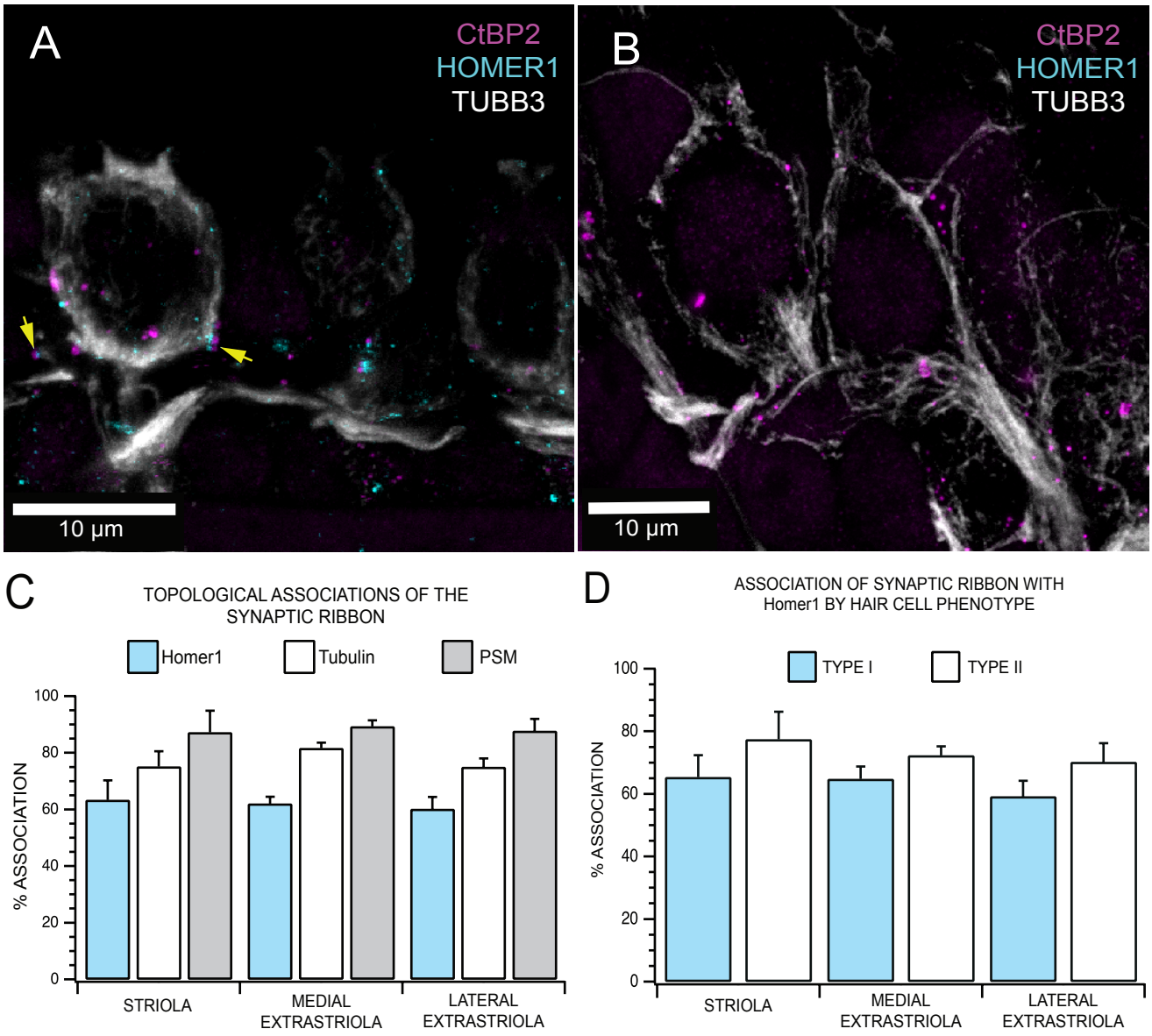

Figure 5. (A) Maximum intensity projection of a substack of optical sections obtained from the striola of a mouse utricle using STED microscopy. CtBP2 (magenta) can be seen in close apposition to Homer1 (cyan) in both type I and type II hair cells. Synapses (yellow arrowheads) can be clearly seen on the inner and outer face of the calyx (β-III tubulin, white), as well as on parent axons (β-III tubulin, white). (B) Maximum intensity projection of a substack of optical sections used as a no primary control for Homer1, showing no labeling in the channel for Homer1, confirming antibody specificity. CtBP2 puncta can be seen within the calyces, apposed to the outer face of the calyces (lateral face projects from type II hair cells), as well as on parent axons (projections from type II hair cells). (C) Topological breakdown of Homer1 associations across the topology of the murine utricle. Error bars represent standard deviations. No differences were found between ribbons associations with Homer1 across the topology of the utricle (Friedman's Test, $p = 0.72$). (D) Associations of ribbons found within each hair cell phenotype with Homer1. Error bars represent standard deviations of the mean. There were no differences in Homer1 association between ribbons located within the two hair cell phenotypes (Friedman's Test, $p = 0.08$).

Figure 6.

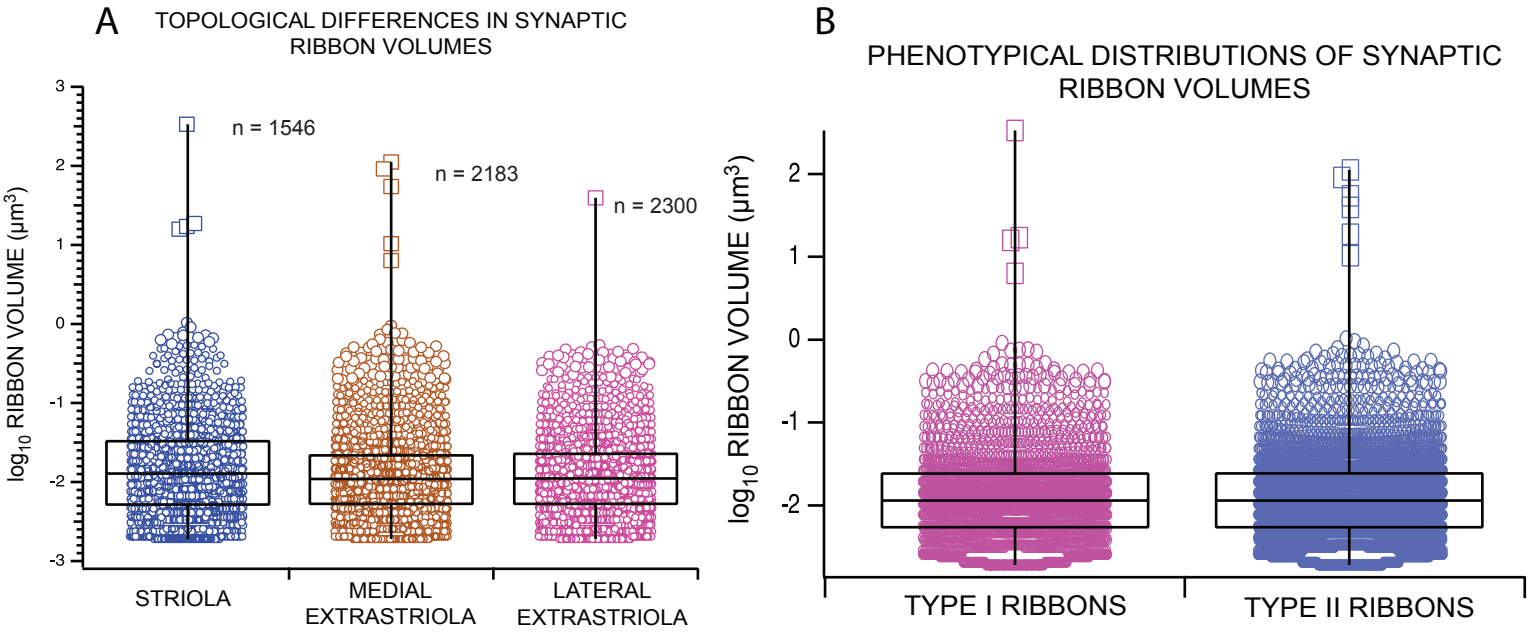

Figure. 6 (A) Box and Whisker Plot displaying the range of ribbon volumes across the different topological regions sampled. The different regions were observed to have differences in the computed ribbon volumes (Kruskal-Wallis, H_0 = 20.7977, H_{crit} = 13.8098, $p < 0.001$). Ribbons located within hair cells of the striola had larger ribbon volumes than those within the medial extrastriola (Non Parametric Multiple Comparison Test, Dunn-Holland Wolfe, Q_t = 4.29859, Q_c = 3.58791, $p < 0.001$) and the lateral extrastriola (Non Parametric Multiple Comparison Test, Dunn-Holland Wolfe, Q_t = 3.77128, Q_c = 3.58791, $p < 0.001$). No difference was found between ribbon volumes of the medial extrastriola and lateral extrastriola (Non Parametric Multiple Comparison Test, Dunn-Holland Wolfe, Q_t = 0.631074, Q_c = 3.58791, $p > 0.001$). (B) Box and Whisker Plot depicting the range of ribbon volumes between Type I and Type II hair cells throughout the utricle. No significant differences were observed between the groups (Kruskal - Wallis, H_0 = 0.227683, H_{crit} = 0.633247, $p > 0.05$).

REFERENCES

1. Blackwell, D. L., Lucas, J. W., & Clarke, T. C. (2014). Summary health statistics for U.S. adults: national health interview survey, 2012. *Vital Health Stat 10*(260), 1-161. https://www.ncbi.nlm.nih.gov/pubmed/24819891
2. Braude, J. P., Vijayakumar, S., Baumgarner, K., Laurine, R., Jones, T. A., Jones, S. M., & Pyott, S. J. (2015). Deletion of Shank1 has minimal effects on the molecular composition and function of glutamatergic afferent postsynapses in the mouse inner ear. Hear Res, 321, 52-64. https://doi.org/10.1016/j.heares.2015.01.008
3. Brosel, S., Laub, C., Averdam, A., Bender, A., & Elstner, M. (2016). Molecular aging of the mammalian vestibular system. *Ageing Res Rev*, 26, 72-80. https://doi.org/10.1016/j.arr.2015.12.007
4. Cassel, R., Bordiga, P., Carcaud, J., Simon, F., Beraneck, M., Le Gall, A., Benoit, A., Bouet, V., Philoxene, B., Besnard, S., Watabe, I., Pericat, D., Hautefort, C., Assie, A., Tonetto, A., Dyhrfjeld-Johnsen, J., Llorens, J., Tighilet, B., & Chabbert, C. (2019). Morphological and functional correlates of vestibular synaptic deafferentation and repair in a mouse model of acute-onset vertigo. *Dis Model Mech*, 12(7). https://doi.org/10.1242/dmm.039115
5. Contini, D., Price, S. D., & Art, J. J. (2017). Accumulation of K(+) in the synaptic cleft modulates activity by influencing both vestibular hair cell and calyx afferent in the turtle. *J Physiol*, 595(3), 777-803. https://doi.org/10.1113/JP273060
6. Contini, D., Zampini, V., Tavazzani, E., Magistretti, J., Russo, G., Prigioni, I., & Masetto, S. (2012). Intercellular K(+) accumulation depolarizes Type I vestibular hair cells and their associated afferent nerve calyx. *Neuroscience*, 227, 232-246. https://doi.org/10.1016/j.neuroscience.2012.09.051
7. Davies, C., Tingley, D., Kachar, B., Wenthold, R. J., & Petralia, R. S. (2001). Distribution of members of the PSD-95 family of MAGUK proteins at the synaptic region of inner and outer hair cells of the guinea pig cochlea. Synapse, 40(4), 258-268. https://doi.org/10.1002/syn.1048

8. Desai, S. S., Zeh, C., & Lysakowski, A. (2005). Comparative morphology of rodent vestibular periphery. I. Saccular and utricular maculae. *J Neurophysiol*, 93(1), 251-266. https://doi.org/10.1152/jn.00746.2003
9. Fernandez, C., Baird, R. A., & Goldberg, J. M. (1988). The vestibular nerve of the chinchilla. I. Peripheral innervation patterns in the horizontal and superior semicircular canals. J Neurophysiol, 60(1), 167-181. https://doi.org/10.1152/jn.1988.60.1.167
10. Fernandez, C., Goldberg, J. M., & Baird, R. A. (1990). The vestibular nerve of the chinchilla. III. Peripheral innervation patterns in the utricular macula. J Neurophysiol, 63(4), 767-780. https://doi.org/10.1152/jn.1990.63.4.767
11. Foster, C. A., & Breeze, R. E. (2013). The Meniere attack: an ischemia/reperfusion disorder of inner ear sensory tissues. *Med Hypotheses*, 81(6), 1108-1115. https://doi.org/10.1016/j.mehy.2013.10.015
12. Goldberg, J. M., Desmadryl, G., Baird, R. A., & Fernandez, C. (1990). The vestibular nerve of the chinchilla. IV. Discharge properties of utricular afferents. J Neurophysiol, 63(4), 781-790. https://doi.org/10.1152/jn.1990.63.4.781
13. Goldberg, J. M., Desmadryl, G., Baird, R. A., & Fernandez, C. (1990). The vestibular nerve of the chinchilla. V. Relation between afferent discharge properties and peripheral innervation patterns in the utricular macula. J Neurophysiol, 63(4), 791-804. https://doi.org/10.1152/jn.1990.63.4.791
14. Gomez-Casati, M. E., Murtie, J. C., Rio, C., Stankovic, K., Liberman, M. C., & Corfas, G. (2010). Nonneuronal cells regulate synapse formation in the vestibular sensory epithelium via erbB-dependent BDNF expression. *Proc Natl Acad Sci U S A*, 107(39), 17005-17010. https://doi.org/10.1073/pnas.1008938107
15. Govindaraju, A. C., Quraishi, I. H., Lysakowski, A., Eatock, R. A., & Raphael, R. M. (2023). Nonquantal transmission at the vestibular hair cell-calyx synapse: K(LV) currents modulate fast

electrical and slow K(+) potentials. *Proc Natl Acad Sci U S A*, 120(2), e2207466120. https://doi.org/10.1073/pnas.2207466120

16. Guth, P. S., Holt, J. C., Perin, P., Athas, G., Garcia, M., Puri, A., Zucca, G., Botta, L., & Valli, P. (1998). The metabotropic glutamate receptors of the vestibular organs. Hear Res, 125(1-2), 154-162. https://doi.org/10.1016/s0378-5955(98)00145-2
17. Halmagyi, G. M., Weber, K. P., & Curthoys, I. S. (2010). Vestibular function after acute vestibular neuritis. *Restor Neurol Neurosci*, 28(1), 37-46. https://doi.org/10.3233/RNN-2010-0533
18. Hickox, A. E., & Liberman, M. C. (2014). Is noise-induced cochlear neuropathy key to the generation of hyperacusis or tinnitus? *J Neurophysiol*, 111(3), 552-564. https://doi.org/10.1152/jn.00184.2013
19. Hoffman, L. F., Choy, K. R., Sultemeier, D. R., & Simmons, D. D. (2018). Oncomodulin Expression Reveals New Insights into the Cellular Organization of the Murine Utricle Striola. J Assoc Res Otolaryngol, 19(1), 33-51. https://doi.org/10.1007/s10162-017-0652-6
20. Holt, J. C., Chatlani, S., Lysakowski, A., & Goldberg, J. M. (2007). Quantal and nonquantal transmission in calyx-bearing fibers of the turtle posterior crista. *J Neurophysiol*, 98(3), 1083-1101. https://doi.org/10.1152/jn.00332.2007
21. Hosoya, M., Fujioka, M., Murayama, A. Y., Ozawa, H., Okano, H., & Ogawa, K. (2021). Neuronal development in the cochlea of a nonhuman primate model, the common marmoset. Dev Neurobiol, 81(8), 905-938. https://doi.org/10.1002/dneu.22850
22. Khan, S., & Chang, R. (2013). Anatomy of the vestibular system: a review. *NeuroRehabilitation*, 32(3), 437-443. https://doi.org/10.3233/NRE-130866
23. Khimich, D., Nouvian, R., Pujol, R., Tom Dieck, S., Egner, A., Gundelfinger, E. D., & Moser, T. (2005). Hair cell synaptic ribbons are essential for synchronous auditory signalling. Nature, 434(7035), 889-894. https://doi.org/10.1038/nature03418

24. Klotz, L., Wendler, O., Frischknecht, R., Shigemoto, R., Schulze, H., & Enz, R. (2019). Localization of group II and III metabotropic glutamate receptors at pre- and postsynaptic sites of inner hair cell ribbon synapses. *FASEB J*, 33(12), 13734-13746. https://doi.org/10.1096/fj.201901543R
25. Kujawa, S. G., & Liberman, M. C. (2009). Adding insult to injury: cochlear nerve degeneration after "temporary" noise-induced hearing loss. *J Neurosci*, 29(45), 14077-14085. https://doi.org/10.1523/JNEUROSCI.2845-09.2009
26. Liberman, L. D., Wang, H., & Liberman, M. C. (2011). Opposing gradients of ribbon size and AMPA receptor expression underlie sensitivity differences among cochlear-nerve/hair-cell synapses. *J Neurosci,* 31(3), 801-808. https://doi.org/10.1523/JNEUROSCI.3389-10.2011
27. Martinez-Monedero, R., Liu, C., Weisz, C., Vyas, P., Fuchs, P. A., & Glowatzki, E. (2016). GluA2-Containing AMPA Receptors Distinguish Ribbon-Associated from Ribbonless Afferent Contacts on Rat Cochlear Hair Cells. *eNeuro*, 3(2). https://doi.org/10.1523/ENEURO.0078-16.2016
28. Michanski, S., Henneck, T., Mukhopadhyay, M., Steyer, A. M., Gonzalez, P. A., Grewe, K., Ilgen, P., Gultas, M., Fornasiero, E. F., Jakobs, S., Mobius, W., Vogl, C., Pangrsic, T., Rizzoli, S. O., & Wichmann, C. (2023). Age-dependent structural reorganization of utricular ribbon synapses. *Front Cell Dev Biol*, 11, 1178992. https://doi.org/10.3389/fcell.2023.1178992
29. Neuhauser, H. K. (2016). The epidemiology of dizziness and vertigo. *Handb Clin Neurol, 137*, 67-82. https://doi.org/10.1016/B978-0-444-63437-5.00005-4
30. Rauch, S. D. (2001). Vestibular histopathology of the human temporal bone. What can we learn? *Ann N Y Acad Sci*, 942, 25-33. https://doi.org/10.1111/j.1749-6632.2001.tb03732.x
31. Ross, M. D. (1994). A spaceflight study of synaptic plasticity in adult rat vestibular maculas. Acta Otolaryngol Suppl, 516, 1-14. https://www.ncbi.nlm.nih.gov/pubmed/7976320

32. Ross, M. D. (2000). Changes in ribbon synapses and rough endoplasmic reticulum of rat utricular macular hair cells in weightlessness. Acta Otolaryngol, 120(4), 490-499. https://doi.org/10.1080/000164800750045983
33. Sadeghi, S. G., Pyott, S. J., Yu, Z., & Glowatzki, E. (2014). Glutamatergic signaling at the vestibular hair cell calyx synapse. *J Neurosci,* 34(44), 14536-14550. https://doi.org/10.1523/JNEUROSCI.0369-13.2014
34. Schmitz, F., Konigstorfer, A., & Sudhof, T. C. (2000). RIBEYE, a component of synaptic ribbons: a protein's journey through evolution provides insight into synaptic ribbon function. *Neuron*, 28(3), 857-872. https://doi.org/10.1016/s0896-6273(00)00159-8
35. Sergeyenko, Y., Lall, K., Liberman, M. C., & Kujawa, S. G. (2013). Age-related cochlear synaptopathy: an early-onset contributor to auditory functional decline. *J Neurosci*, 33(34), 13686-13694. https://doi.org/10.1523/JNEUROSCI.1783-13.2013
36. Sobkowicz, H. M., Rose, J. E., Scott, G. E., & Slapnick, S. M. (1982). Ribbon synapses in the developing intact and cultured organ of Corti in the mouse. *J Neurosci*, 2(7), 942-957. https://doi.org/10.1523/JNEUROSCI.02-07-00942.1982
37. Songer, J. E., & Eatock, R. A. (2013). Tuning and timing in mammalian type I hair cells and calyceal synapses. *J Neurosci*, 33(8), 3706-3724. https://doi.org/10.1523/JNEUROSCI.4067-12.2013
38. Spaiardi, P., Marcotti, W., Masetto, S., & Johnson, S. L. (2022). Signal transmission in mature mammalian vestibular hair cells. Front Cell Neurosci, 16, 806913. https://doi.org/10.3389/fncel.2022.806913
39. Stamataki S, Francis HW, Lehar M, May BJ & Ryugo DK (2006). Synaptic alterations at inner hair cells precede spiral ganglion cell loss in aging C57BL/6J mice. *Hear Res* **221**, 104–118.
40. Sultemeier, D. R., Choy, K. R., Schweizer, F. E., & Hoffman, L. F. (2017). Spaceflight-induced synaptic modifications within hair cells of the mammalian utricle. *J Neurophysiol*, 117(6), 2163-2178. https://doi.org/10.1152/jn.00240.2016

41. Sultemeier, D. R., & Hoffman, L. F. (2017). Partial Aminoglycoside Lesions in Vestibular Epithelia Reveal Broad Sensory Dysfunction Associated with Modest Hair Cell Loss and Afferent Calyx Retraction. *Front Cell Neurosci*, 11, 331. https://doi.org/10.3389/fncel.2017.00331
42. Tu, J. C., Xiao, B., Yuan, J. P., Lanahan, A. A., Leoffert, K., Li, M., Linden, D. J., & Worley, P. F. (1998). Homer binds a novel proline-rich motif and links group 1 metabotropic glutamate receptors with IP3 receptors. *Neuron*, 21(4), 717-726. https://doi.org/10.1016/s0896-6273(00)80589-9
43. Vasilkov, V., Caswell-Midwinter, B., Zhao, Y., de Gruttola, V., Jung, D. H., Liberman, M. C., & Maison, S. F. (2023). Evidence of cochlear neural degeneration in normal-hearing subjects with tinnitus. *Sci Rep*, 13(1), 19870. https://doi.org/10.1038/s41598-023-46741-5
44. Viana, L. M., O'Malley, J. T., Burgess, B. J., Jones, D. D., Oliveira, C. A., Santos, F., Merchant, S. N., Liberman, L. D., & Liberman, M. C. (2015). Cochlear neuropathy in human presbycusis: Confocal analysis of hidden hearing loss in post-mortem tissue. *Hear Res*, 327, 78-88. https://doi.org/10.1016/j.heares.2015.04.014
45. Voorn, R. A., & Vogl, C. (2020). Molecular Assembly and Structural Plasticity of Sensory Ribbon Synapses—A Presynaptic Perspective. *International Journal of Molecular Sciences*, 21(22), 8758. https://www.mdpi.com/1422-0067/21/22/8758
46. Wan, G., Ji, L., Schrepfer, T., Gong, S., Wang, G. P., & Corfas, G. (2019). Synaptopathy as a Mechanism for Age-Related Vestibular Dysfunction in Mice. *Front Aging Neurosci*, 11, 156. https://doi.org/10.3389/fnagi.2019.00156
47. Wu PZ, Liberman LD, Bennett K, de Gruttola V, O'Malley JT, Liberman MC (2019). Primary neural degeneration in the human cochlea: evidence for hidden hearing loss in the aging ear. *Neurosci* 407, 8–20.
48. Xiao, B., Tu, J. C., Petralia, R. S., Yuan, J. P., Doan, A., Breder, C. D., Ruggiero, A., Lanahan, A. A., Wenthold, R. J., & Worley, P. F. (1998). Homer regulates the association of group 1

metabotropic glutamate receptors with multivalent complexes of homer-related, synaptic proteins. *Neuron*, 21(4), 707-716. https://doi.org/10.1016/s0896-6273(00)80588-7

49. Yamasoba, T., Lin, F. R., Someya, S., Kashio, A., Sakamoto, T., & Kondo, K. (2013). Current concepts in age-related hearing loss: epidemiology and mechanistic pathways. *Hear Res*, 303, 30-38. https://doi.org/10.1016/j.heares.2013.01.021
50. Yoon, S., Piguel, N. H., Khalatyan, N., Dionisio, L. E., Savas, J. N., & Penzes, P. (2021). Homer1 promotes dendritic spine growth through ankyrin-G and its loss reshapes the synaptic proteome. *Mol Psychiatry*, 26(6), 1775-1789. https://doi.org/10.1038/s41380-020-00991-1
51. Zanazzi, G., & Matthews, G. (2009). The molecular architecture of ribbon presynaptic terminals. *Mol Neurobiol*, 39(2), 130-148. https://doi.org/10.1007/s12035-009-8058-z